

ALMASOP: Inner-Envelope Structures of Protostars Driving Nascent Jets

SOMNATH DUTTA ,¹ CHIN-FEI LEE ,¹ NAOMI HIRANO ,¹ DOUG JOHNSTONE ,^{2,3} KEE-TAE KIM ,^{4,5} YI-JEHNG KUAN ,^{6,1} JAMES DI FRANCESCO,^{2,3} KEN'ICHI TATEMATSU ,^{7,8} MIKA JUVELA ,⁹ CHANG WON LEE,^{4,5} ALESSIO TRAFICANTE,¹⁰ VIVIEN HUEI-RU CHEN,¹¹ MANASH RANJAN SAMAL,¹² DAVID EDEN,¹³ DIPEN SAHU ,^{12,1} SHIH-YING HSU ,¹ TIE LIU ,¹⁴ AND SHENG-YUAN LIU

¹*Academia Sinica Institute of Astronomy and Astrophysics, Roosevelt Rd, Taipei 106319, Taiwan, R.O.C.*

²*NRC Herzberg Astronomy and Astrophysics, 5071 West Saanich Rd, Victoria, BC, V9E 2E7, Canada*

³*Department of Physics and Astronomy, University of Victoria, Victoria, BC, V8P 5C2, Canada*

⁴*Korea Astronomy and Space Science Institute (KASI), 776 Daedeokdae-ro, Yuseong-gu, Daejeon 34055, Republic of Korea*

⁵*University of Science and Technology, Korea (UST), 217 Gajeong-ro, Yuseong-gu, Daejeon 34113, Republic of Korea*

⁶*Department of Earth Sciences, National Taiwan Normal University, Taipei, Taiwan, R.O.C.*

⁷*Nobeyama Radio Observatory, National Astronomical Observatory of Japan, National Institutes of Natural Sciences, 462-2 Nobeyama, Minamimaki, Minamisaku, Nagano 384-1305, Japan*

⁸*Department of Astronomical Science, SOKENDAI (The Graduate University for Advanced Studies), 2-21-1 Osawa, Mitaka, Tokyo 181-8588, Japan*

⁹*Department of Physics, P.O.Box 64, FI-00014, University of Helsinki, Finland*

¹⁰*IAPS-INAF, via Fosso del Cavaliere 100, I-00133, Rome, Italy*

¹¹*Institute of Astronomy and Department of Physics, , National Tsing Hua University, Hsinchu, 300044, Taiwan*

¹²*Physical Research Laboratory, Navrangpura, Ahmedabad, Gujarat 380009, India*

¹³*Armagh Observatory and Planetarium, College Hill, Armagh, BY61 9DB, United Kingdom*

¹⁴*Shanghai Astronomical Observatory, Chinese Academy of Sciences, 80 Nandan Road, Shanghai 200030, China*

ABSTRACT

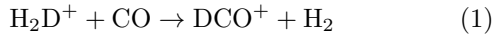
Protostellar jets provide valuable insight into the evolutionary stage and formation history of star-forming cores in their earliest phases. We investigated the inner envelope structures of three extremely young protostars, selected for having the shortest dynamical timescales in their outflows and jets. Our analysis is based on Atacama Large Millimeter/submillimeter Array (ALMA) observations of the N₂D⁺, DCO⁺, DCN, C¹⁸O, CH₃OH, and H₂CO lines, along with 1.3 mm continuum data, obtained at two spatial resolutions of \sim 500 AU and 150 AU. By examining molecular depletion and sublimation patterns, emission extents at core-scale and outflow rotational temperatures, we assessed the relative evolutionary stages of the three sources. In G208.68-19.20N1, the absence of N₂D⁺ toward the core—despite a semi-ring-like distribution—and the presence of bright DCN and DCO⁺ emission co-spatial with C¹⁸O indicate a warmer envelope, possibly suggesting a more advanced evolutionary state. In contrast, G208.68-19.20N3 shows no dense central structures in C¹⁸O, DCN, DCO⁺, or N₂D⁺, with emission instead appearing scattered around the continuum and along large-scale filaments, consistent with a likely younger stage than G208.68-19.20N1. The third source, G215.87-17.62M, exhibits compact C¹⁸O emission at the continuum peak, but spatially extended N₂D⁺, DCN, and DCO⁺ along the continuum, pointing to a cooler envelope and likely the youngest stage among the three. This comparative analysis across three protostars demonstrates the effectiveness of molecular tracers for evolutionary staging, though variations in luminosity or accretion may also shape chemical morphologies. These results highlight the promise of broader surveys for advancing our understanding of early protostellar evolution.

Keywords: Protostars (1302) — Stellar jets (1607) — Submillimeter astronomy (1647) — Astrochemistry (75) — Circumstellar envelopes (237) — Star formation (1569)

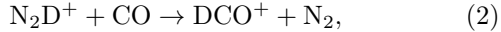
1. INTRODUCTION

The internal structure of the envelope in the earliest phases of protostellar evolution offers a unique window into the initial environmental conditions shaping core development. During this stage, increasing central luminosity raises core temperatures, heating the surrounding material and driving chemical evolution. A detailed investigation of the envelope's chemical structure at this phase is therefore crucial for understanding the processes governing early protostellar evolution.

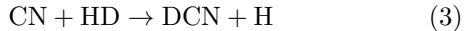
Different molecular species in protostellar cores can be correlated through their depletion, sublimation, temperature dependence, and spatial distribution of emission. For example, deuterated species like N_2D^+ show enhanced fractional abundance in cores on the verge of stellar collapse, when the gas temperature is ~ 10 K (e.g., Caselli et al. 1999; Sipilä et al. 2015; Kim et al. 2020; Li et al. 2022). As the core evolves and the surrounding gas is heated above the CO sublimation temperature (~ 25 K), molecular species synthesized from sublimated CO become detectable. Gas-phase CO can produce DCO^+ by destroying H_2D^+ or N_2D^+ via



and



respectively (e.g., Caselli et al. 1999; Lee et al. 2004). DCN can also form in warmer gas, where thermal desorption releases it from icy grain mantles into the gas phase. In outflows or accretion shocks ($T > 100$ K), neutral-neutral reactions such as



become important for DCN production (e.g., Flower et al. 2006). Consequently, N_2D^+ depletion is expected in regions of high CO abundance, accompanied by enhanced DCO^+ and DCN emission (e.g., Jansen et al. 1995; Parise et al. 2009). Thus, the detection, depletion, and sublimation of specific molecular species diagnose local heating and the evolutionary status of protostellar cores, and Atacama Large Millimeter/submillimeter Array (ALMA) observations of dense gas tracers at submillimeter wavelengths are crucial for revealing the morphology, kinematics, and chemical composition of their high-density envelopes.

Protostellar jets are launched at the onset of collapse and serve as signposts of the accretion process (e.g.,

Reipurth & Bally 2001; Frank et al. 2014; Bally 2016; Lee 2020). In the earliest stages, the high density of circumstellar material confines the jets within the envelope (e.g., Arce et al. 2007), resulting in smaller spatial extents and younger dynamical ages (e.g., Bontemps et al. 1996; Dutta et al. 2024). Consequently, protostellar systems hosting the youngest jets provide unique laboratories for probing freshly formed molecules in the immediate vicinity of the protostar, offering insights into the earliest stages of chemical and dynamical evolution.

In this paper, we investigate the envelopes of three protostars — G208.68-19.20N1 (G208N1, also known as HOPS 87), G208.68-19.20N3 (G208N3), and G215.87-17.62M (G215M) — which exhibit molecular SiO and CO emission in their high-density jets, indicative of young jet activity. These sources are located within the Orion molecular cloud complex. The morphology of their jets has been examined in Dutta et al. (2024) through SiO and CO emission using ALMA observations, as part of the ALMASOP project (ALMA Survey of Orion Planck Galactic Cold Clumps; Dutta et al. 2020). Table 1 outlines the main characteristics of the protostars. G208N1 is a Class 0 protostar with $T_{\text{bol}} = 38 \pm 13$ K and $L_{\text{bol}} = 36.7 \pm 14.5 L_{\odot}$ (Furlan et al. 2016; Tobin et al. 2020; Dutta et al. 2020), and from 1.3 mm continuum observations at ~ 2000 AU resolution, its envelope mass was derived to be $M_{\text{env}} \approx 8.26 \pm 1.28 M_{\odot}$. G208N3, located $\sim 16''$ from a close binary system (N3B and N3C) (Dutta et al. 2020), remains poorly characterized in earlier studies with no estimates of T_{bol} or L_{bol} reported; however, continuum data yield an envelope mass of $M_{\text{env}} \sim 2.08 \pm 0.34 M_{\odot}$. G215M is the least studied of the three, with no T_{bol} or L_{bol} estimates available, and its envelope mass is measured as $M_{\text{env}} \sim 0.30 \pm 0.07 M_{\odot}$. Based on the spatial extents and deprojected velocities of the three jets, as determined by Dutta et al. (2024), these protostars appear to have extremely young dynamical ages (< 500 yr) and moderately high jet mass-loss rates of $(0.3-2.5) \times 10^{-6} M_{\odot} \text{ yr}^{-1}$. These characteristics make them excellent examples of extremely young protostellar systems that have only recently begun their accretion-driven outflow activity. Studying such objects provides valuable insight into the physical and chemical conditions at the earliest stages of protostellar evolution. The structure of the paper is as follows: Section 2 describes the data used in this study; Section 3 presents

Table 1. Observed Parameters of the Protostars

Parameter	G208N1	G208N3	G215M	References
T_{bol} (K)	38 ± 13	¹ , ² , ³
L_{bol} (L_{\odot})	36.7 ± 14.5	¹ , ² , ³
M_{env} (M_{\odot})	8.26 ± 1.28	2.08 ± 0.34	0.30 ± 0.07	⁴
$R_{\text{env@500AU}}$ (AU)	4000–5000	1200–2000	1000–2400	This study
\dot{M}_{jet} ($10^{-6} M_{\odot} \text{ yr}^{-1}$)	2.5	1.3	0.32	⁴
V_{jet} (km s^{-1})	102^{+24}_{-35}	61^{+41}_{-15}	60^{+28}_{-13}	⁴
F_{CO} ($10^{-6} \text{ km s}^{-1} \text{ yr}^{-1}$)	2.54	1.70	1.15	⁴
τ_{dyn} (yr)	47^{+38}_{-10}	228^{+160}_{-110}	292^{+133}_{-108}	⁴
T_{rot} (K)	75–164	110–193	50–54	This study

¹[Furlan et al. \(2016\)](#)²[Dutta et al. \(2020\)](#)³[Tobin et al. \(2020\)](#)⁴[Dutta et al. \(2024\)](#)

the observational results; Section 4 discusses the evolutionary status of the sources; and Section 5 summarizes our findings and presents the main conclusions.

2. OBSERVATIONS

2.1. *Data from ALMASOP*

We have utilized ALMA archive data observed as a part of the ALMA Survey of Orion Planck cold clumps (ALMASOP; Project ID:2018.1.00302.S) in Band 6 (see [Dutta et al. 2020](#), for more details on ALMASOP). In this paper, we make use of C^{18}O , N_2D^+ , DCN , DCO^+ , CH_3OH , and H_2CO . For CH_3OH we have studied two transitions at CH_3OH (4₂ – 3₁) and CH_3OH (10₂ – 9₃). For H_2CO , we have created maps at three transitions H_2CO 3(0, 3) – 2(0, 2), H_2CO 3(2, 2) – 2(2, 1) and H_2CO 3(2, 1) – 2(2, 0). Following [Dutta et al. \(2024\)](#), we reproduced CO (2–1) and SiO (5–4) maps. Although additional lines are detected toward some individual protostars, we selected the present set of transitions because they are the most common molecular tracers in young protostars, and are well suited to probe both the envelope and outflow components. They are detected in the majority of our studied sources. While a few lines are missing in certain objects, these absences are themselves scientifically meaningful and provide additional insight into the diversity of physical and chemical conditions across our sample. The spectral lines used in this work, along with their rest frequency (ν), upper-state energy (E_{up}), and logarithmic Einstein coefficient (A_{ul}), are listed in Table 2. The spectroscopic parameters were adopted from the laboratory measurements

reported in the literature (e.g., [Müller et al. 2000, 2001](#); [Endres et al. 2016](#); [Müller & Lewen 2017](#)), as compiled in the Cologne Database for Molecular Spectroscopy (CDMS; [Müller et al. 2005](#)) and made available through the Splatatalogue database¹. Data calibration has been performed with the standard pipeline in CASA 5.5 ([McMullin et al. 2007](#)). We have generated two sets of line cubes for all transitions and continuum emission: (i) by combining all visibilities observed with 12 m C43-5 (TM1), 12 m C43-2 (TM2), and 7 m ACA (see [Dutta et al. 2020](#), for more details), where the synthesized beam size is $\sim 0''.41 \times 0''.34$, and (ii) with a UV taper of $\sim 1''.0$ by combining all visibilities (TM1+TM2+ACA), which leads to synthesize beam size of $\sim 1''.5 \times 1''.2$. Throughout this paper, we refer to the first case as high-resolution (~ 150 AU at Orion distance) and the latter as low-resolution (~ 500 AU at Orion distance). The combined maps of TM1+TM2+ACA have a maximum recoverable scale (MRS) of $\sim 14''$. In all cases, we have applied a robust weighting factor of $R_w = +2.0$ (natural weighting) to enhance sensitivity to extended emission. The line cube channels were binned to 2 km s^{-1} to improve sensitivity. The continuum peak positions at high resolution, together with the continuum sensitivities and the mean per-channel sensitivity of the line cubes at both high and low resolution, are listed in Table 3. The ALMA flux calibration uncertainty is estimated

¹ <https://splatatalogue.online/>

to be $\sim 10\%$, consistent with standard values for Band 6 observations.

2.2. Data from the ALMA Archive

We have retrieved ALMA band 6 data observed in Cycle-3 (#2015.1.00341.S; PI; S. Takahashi) at high spectral resolution. Among the three objects studied here, two were included in this project G208.68-19.20N1 as MMS6 and G208.68-19.20N3 as MMS2. The SPW, which includes N_2D^+ line, was set to the high spectral resolution mode with a 35.28 kHz resolution and the corresponding velocity resolution was $\sim 0.046 \text{ km s}^{-1}$. The N_2D^+ images were created using the data observed with the ACA 7m array and C36-1 configuration of the 12m array. The visibility data were calibrated using CASA.

The calibrated visibility data from the two configurations were combined and imaged with the TCLEAN task in CASA 5.5, after continuum subtraction, to produce a line image cube. We applied Briggs weighting with a robust parameter of +0.5. Further details of the data reduction are provided in Hirano et al. (2024). The final N_2D^+ image cubes have a synthesized beam of $\sim 1''.5 \times 0''.9$, a velocity resolution of $\sim 0.1 \text{ km s}^{-1}$, and a per-channel sensitivity of $\sim 33 \text{ mJy beam}^{-1}$. These archival observations have a similar resolution and recoverable scale to the ALMASOP low-resolution 1'' UV-tapered maps, although they have a significantly higher velocity resolution (~ 20 times) compared with ALMASOP. The absolute flux calibration uncertainty of these Band 6 observations is $\sim 10\%$, based on the ALMA calibrator measurements.

3. RESULTS

3.1. Dense Gas Tracers around the envelope

Multiple molecular tracers of the gas surrounding the protostellar envelopes are shown in Figure 1 at a low resolution of $\sim 500 \text{ AU}$, and in Figure 2 at a higher resolution of $\sim 150 \text{ AU}$. Each figure consists of three columns, corresponding to the three target sources. The background images show integrated molecular line maps, with the velocity ranges indicated in each panel. We consider the integrated emission to be detected when the emission in the integrated maps exceeds 3σ . The maps are produced by integrating over velocity channels where the emission in each channel exceeds the 3σ level. Overlaid in magenta are continuum contours at comparable resolution, tracing primarily the dust emission. The jet axes, determined from the CO and SiO emission (Figure A1), are shown as arrows. In the following sections, we describe the envelope morphology for each of the three objects, highlighting the contributions

of different molecular tracers and dust emission across both spatial scales, from lower to higher resolution.

G208N1 (first column of Figure 1 and 2) is embedded within a large C^{18}O core at a resolution of $\sim 500 \text{ AU}$; although compact in appearance, the C^{18}O peak lies northeast of the continuum peak (Figure 1). A close-up view of the high-resolution ($\sim 150 \text{ AU}$) C^{18}O map shows that the emission near the source is elongated along the outflow axis ($\text{PA} \sim 175^\circ$; see Section A), with a central gap coincident with the 1.3 mm continuum peak (Figure 2). Compact $\text{CH}_3\text{OH}(10_2 - 9_3)$ emission is detected within the inner region of the 1.3 mm continuum, and the high-resolution $\text{CH}_3\text{OH}(10_2 - 9_3)$ map reveals structures likely tracing the jet base. Notably, N_2D^+ is either absent or significantly depleted near the protostellar core, forming an arc-like boundary from the north through east to south around the continuum peak. The DCN emission is more extended at $\sim 500 \text{ AU}$ resolution; in the high-resolution ($\sim 150 \text{ AU}$) maps it becomes concentrated at the continuum peaks and is predominantly distributed near the jet base. This suggests that DCN emission may occupy regions left vacant by the absence of N_2D^+ . Finally, DCO^+ shows an anticorrelation with C^{18}O on both spatial scales: at low resolution it is relatively extended, while at high resolution it is concentrated mainly at the continuum peak. From a visual inspection of the molecular line and continuum emission maps at $\sim 500 \text{ AU}$ resolution, we estimate that the envelope has an approximate diameter of 4000–6000 AU.

G208N3 (second column of Figure 1 and 2) exhibits extended C^{18}O emission in the envelope at both high and low spatial scales. $\text{CH}_3\text{OH}(10_2 - 9_3)$ is non-detected around this source. The low-resolution N_2D^+ map suggests that the core is located within a large filamentary cloud elongated from northwest to southeast. In the high-resolution map, N_2D^+ appears scattered along the filaments; a close inspection of the continuum peak indicates that it is mostly scattered and depleted near the continuum peak. Low-resolution maps reveal that the bright DCN is elongated along the outflow direction ($\text{PA} \sim 45^\circ$, see Section A), from northeast to southwest near the core. The G208N3 core itself is also situated within a large filamentary cloud that extends similarly to the N_2D^+ emission. In the high-resolution DCN map, the emission forms a partial ring-like structure around the continuum peak toward the west and northeast. At low resolution, DCO^+ shows a filamentary distribution similar to that of N_2D^+ , with three dense cores embedded within the observed DCO^+ filaments; G208N3 is located in one of these dense cores. In the high-resolution maps, DCO^+ emission is more scattered and peaks away from the continuum center,

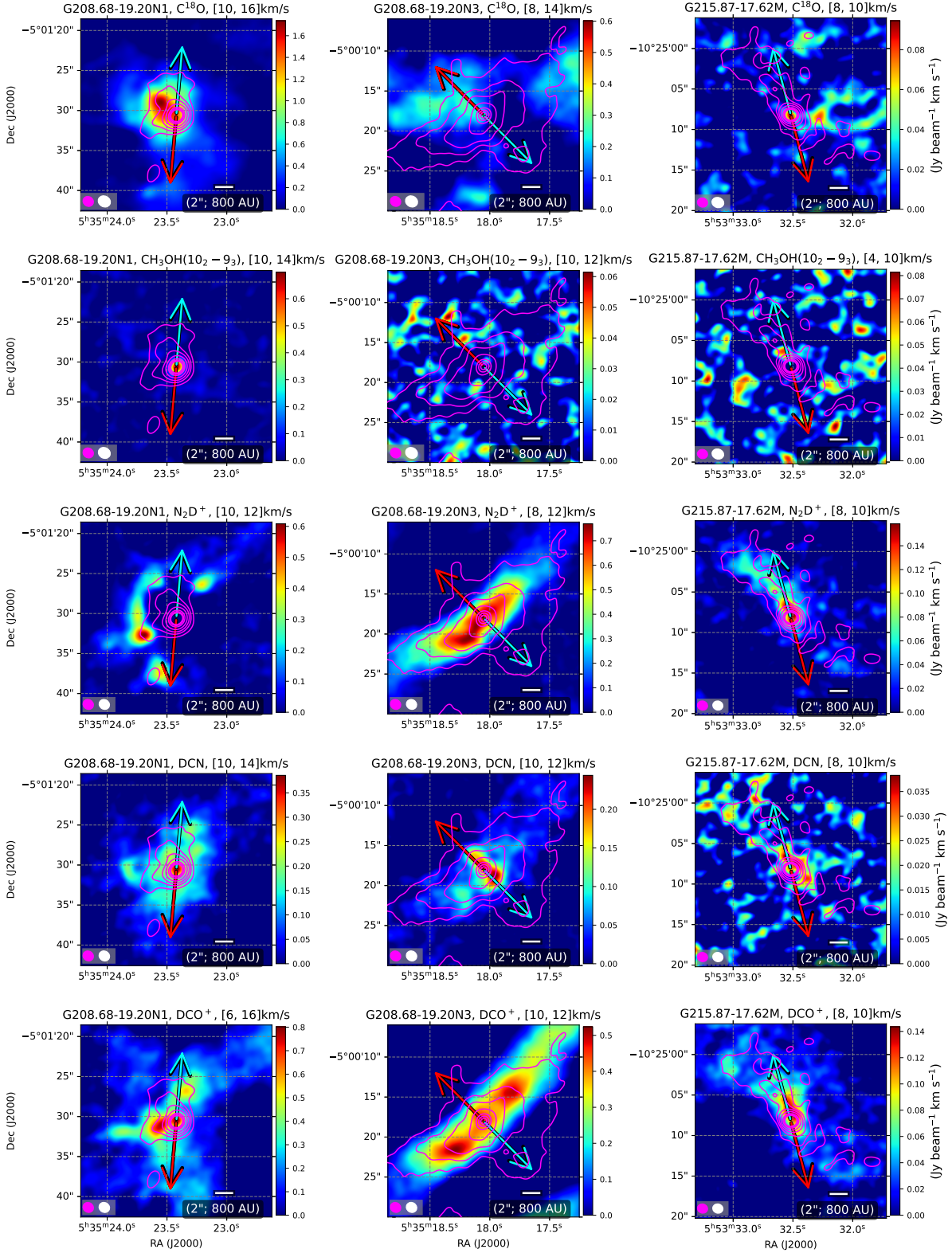


Figure 1. Low-angular resolution maps at a spatial scale of ~ 500 AU are shown for different molecular tracers, primarily tracing the envelope structures. The three columns correspond to three sources: G208.68-19.20N1 (G208N1), G208.68-19.20N3 (G208N3), and G215.87-17.62M (G215M), respectively. The background images display molecular emission maps integrated over the specified velocity ranges indicated at the top of each panel. Magenta contours, plotted at the same angular resolution as the molecular emission, represent the continuum emission at levels of $(6, 18, 36, 72, 144, 200, 250) \times \sigma$, where σ is 1.5, 0.14, and 0.04 mJy beam $^{-1}$ km s $^{-1}$ for G208N1, G208N3, and G215M, respectively. Jet axis directions are indicated with red arrows for redshifted emission and cyan arrows for blueshifted emission. Beam sizes are shown in the lower left of each panel, with magenta representing the continuum and white representing the molecular emission. A spatial scale bar is provided.

Table 2. Spectral lines used in this work

Molecule	Transition	ν (GHz)	E_{up} (K)	$\log_{10}(A_{\text{ul}})$ (s^{-1})
C^{18}O	2–1	219.5603541	15.81	−6.22
N_2D^+	3–2	231.3199064	22.20	−4.05
DCN	3–2	217.2383000	20.85	−3.34
DCO^+	3–2	216.1125705	20.74	−2.62
CH_3OH	4_2-3_1	218.4400630	45.46	−4.33
CH_3OH	10_2-9_3	231.2811100	165.35	−4.74
H_2CO	$3_{0,3}-2_{0,2}$	218.2221920	20.96	−3.55
H_2CO	$3_{2,2}-2_{2,1}$	218.4756320	68.09	−3.80
H_2CO	$3_{2,1}-2_{2,0}$	218.7600660	68.11	−3.80
^{12}CO	2–1	230.5380000	16.60	−6.16
SiO	5–4	217.1049800	31.26	−3.28

Table 3. Continuum Peak Positions and Continuum/Spectral Sensitivities (ALMASOP)

Source	RA (h:m:s)	Dec (d:m:s)	Continuum rms (mJy beam^{-1})		Line rms/channel (mJy beam^{-1})		Vel Res (km s^{-1})
			@150 AU	@500 AU	@150 AU	@500 AU	
G208N1	05:35:23.42	−05:01:30.60	0.20	1.50	3.5	5.8	2
G208N3	05:35:18.06	−05:00:18.19	0.20	0.14	3.4	5.5	2
G215M	05:53:32.52	−10:25:08.18	0.04	0.04	3.2	5.2	2

Table 4. N_2D^+ Fit Parameters

Position	T_{ex} (K)	τ	V_{LSR} (km/s)	V_{FWHM} (km/s)
G208N1				
p1	12.34 ± 1.25	4.63 ± 2.14	10.95 ± 0.02	0.10 ± 0.02
p2	11.18 ± 2.07	2.92 ± 2.44	11.51 ± 0.04	0.20 ± 0.05
p3	10.29 ± 1.84	3.55 ± 2.77	11.47 ± 0.03	0.11 ± 0.03
p4	10.68 ± 7.33	1.60 ± 3.26	11.31 ± 0.05	0.20 ± 0.08
p5	12.82 ± 2.08	3.17 ± 1.93	10.90 ± 0.02	0.12 ± 0.02
G208N3				
p1	21.18 ± 0.54	10.24 ± 1.33	11.11 ± 0.01	0.12 ± 0.01

NOTE—The parameters for position p4 have unusually large uncertainties due to low signal-to-noise in the satellite lines.

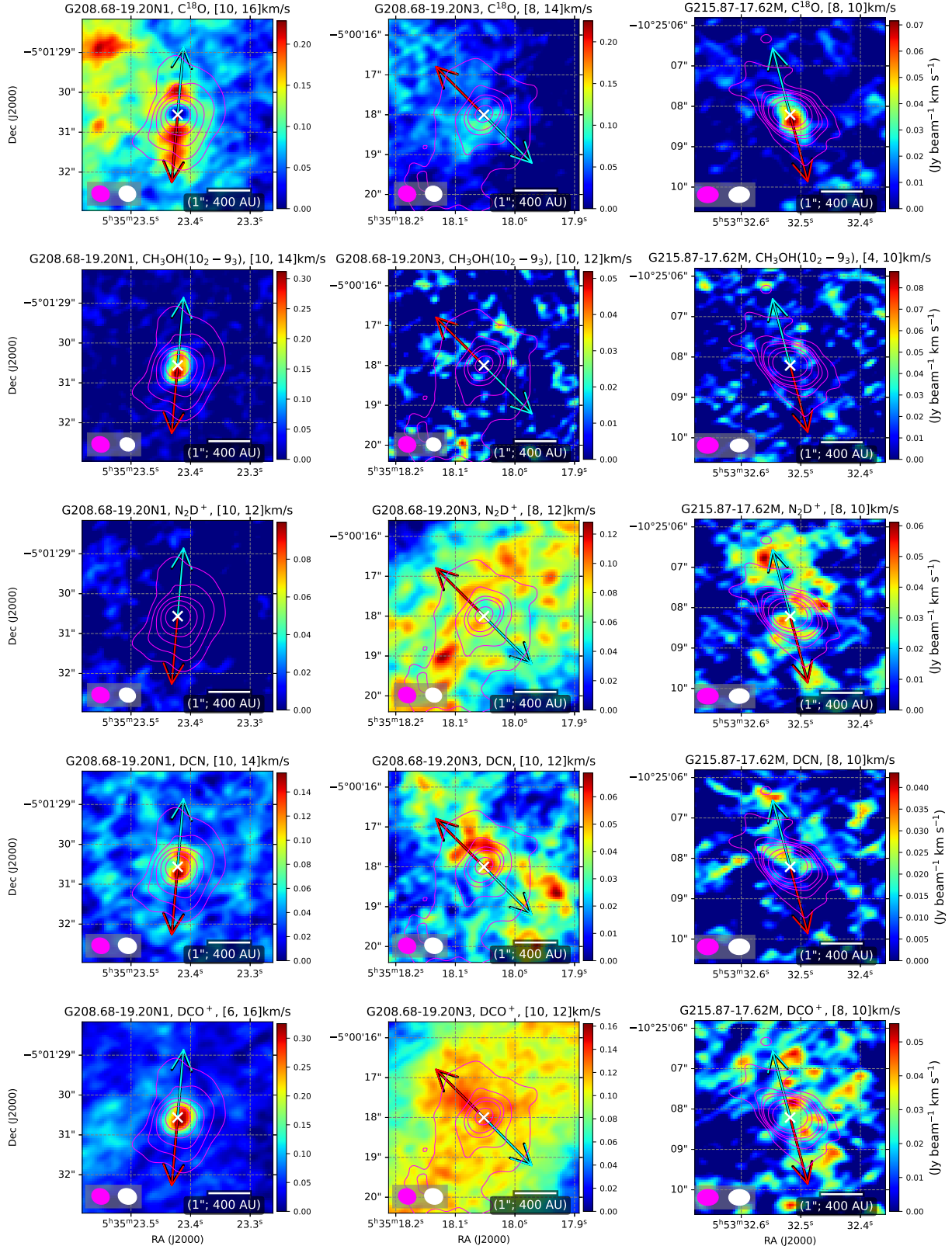


Figure 2. High-angular resolution maps at a spatial scale of ~ 150 AU are shown. All symbols are the same as in Figure 1. The continuum contours, plotted at the same angular resolution as the molecular emission, are at $(50, 100, 200, 400, 800) \times \sigma$ ($\sigma = 0.2$ mJy beam $^{-1}$ km s $^{-1}$) for G208N1, and $(6, 12, 18, 24, 50, 100) \times \sigma$ for G208N3 ($\sigma = 0.2$ mJy beam $^{-1}$ km s $^{-1}$) and for G215M ($\sigma = 0.04$ mJy beam $^{-1}$ km s $^{-1}$). The Continuum peaks are marked with white crosses.

primarily along the northeastern jet axis. Based on a visual inspection of the molecular line emission and continuum extent at resolution of ~ 500 AU, we estimate that the envelope of G208N3 spans a diameter of ~ 1200 – 2000 AU.

G215M (third column of Figures 1 and 2) exhibits compact C^{18}O emission centered on the continuum peak in both the low- and high-resolution maps, with a slight elongation along the jet direction ($\text{PA} \sim 15^\circ$) that is more prominent in the high-resolution map. $\text{CH}_3\text{OH}(10_2 - 9_3)$ is not clearly detected in any of the maps toward the continuum. N_2D^+ emission is present in both spatial scales, appearing extended along the continuum in the low-resolution map. In the high-resolution map, the N_2D^+ emission is more scattered but remains visible around the envelope, extending beyond the 1.3 mm continuum into a filamentary structure. DCN is also detected along the extended continuum emission at low resolution, while in the high-resolution maps it appears only marginally detected as scattered emission. The distribution of DCO^+ closely resembles that of N_2D^+ and DCN. Visual inspection of the molecular and continuum emission at a resolution of ~ 500 AU suggests that the inner envelope has a diameter of ~ 1000 – 2400 AU, excluding the extended emission along the northeast–southwest direction.

3.2. N_2D^+ Emission with Higher Spectral Resolution

High spectral resolution observations of N_2D^+ at ~ 0.1 km s $^{-1}$ have been analyzed to investigate the kinematics and physical properties of the dense gas surrounding two cores, G208N1 and G208N3; these data do not cover G215M. The N_2D^+ line consists of numerous hyperfine (hf) components. Fitting these hyperfine lines allows us to derive key parameters such as the excitation temperature T_{ex} , optical depth τ , LSR velocity V_{LSR} , and line width V_{FWHM} . Figure 3 shows the N_2D^+ spectra for G208N1 and G208N3. The spectra for G208N1 were extracted from regions with a radius of 1''.5 around the peak emission associated with the semi-arc-like envelope structure. Five such peaks, labeled p1–p5, were visually identified around the envelope (Figure 3 and Table 4). These regions correspond to the surrounding envelope and have peak velocities ranging from 10.3 to 11.5 km s $^{-1}$, close to the systemic velocity, with a FWHM of only 0.1–0.2 km s $^{-1}$. The velocity extends from 10 to 12.5 km s $^{-1}$. These locations therefore most likely unrelated to outflow emission, and the emission is not coincident with the outflow or jet axis. For G208N3, the spectrum extraction was performed at the core center, as marked in Figure 3. In all cases, we selected a radius of 1''.5 to ensure that at least one beam size of

emission is included in the spectra. The spectra were fitted using the *pyspeckit* software package with the *n2dp* model. The fitting parameters are overplotted as legends on the figure and listed in Table 4.

G208N1 exhibits excitation temperatures T_{ex} in the range 10–13 K, except for values from position P4, which show large uncertainties and poorly detected satellite lines. All these peaks were detected around the arc-like structure in the envelope, away from the continuum center. In contrast, N_2D^+ traces emission closer to the source in G208N3. Consequently, the excitation temperature (~ 21 K) is higher for G208N3 than for G208N1.

The optical depth in G208N3 ($\sim 10.24 \pm 1.33$) is a few times higher than in G208N1 (in a range ~ 2.9 – 4.0). The satellite groups are brighter in G208N3 than in G208N1, possibly because N_2D^+ in G208N1 has been depleted due to internal heating during its evolution, whereas G208N3 is younger and internal heating is insufficient to cause significant depletion. The LSR velocities are $V_{\text{LSR}} \sim 11.509$ km s $^{-1}$ and 11.134 km s $^{-1}$ for G208N1 and G208N3, respectively. The velocity line widths are similar for both sources.

3.3. Molecular Gas along the Outflows

Figure 4 presents $\text{CH}_3\text{OH}(4_2 - 3_1)$, $\text{H}_2\text{CO} 3(0, 3) - 2(0, 2)$, $\text{H}_2\text{CO} 3(2, 2) - 2(2, 1)$, and $\text{H}_2\text{CO} 3(2, 1) - 2(2, 0)$ emission, which, together with $\text{CO}(2-1)$ and $\text{SiO}(5-4)$ (Figure A1), trace collimated structures along the jet axis. All three sources exhibit similar velocity extents in CO and SiO, as well as comparable spatial morphology, which complicates the distinction between the collimated jet and the outflow (see also Dutta et al. 2024). C^{18}O further traces the jet base near the sources (Figures 2, 1). In all three protostars, emission is detected along the jet axis. As shown earlier, higher CH_3OH transitions peak in the envelope or jet base, while lower transitions such as $\text{CH}_3\text{OH}(4_2 - 3_1)$ are more sensitive to extended jet/outflow emission. H_2CO behaves similarly, appearing both in the envelope and along the outflow.

G208N1 (first row of Figure 4) shows a unipolar jet/outflow extends northward. Low-resolution maps (~ 500 AU; Figure A2), clearly show the outflow, while high-resolution data reveal $\text{CH}_3\text{OH}(4_2 - 3_1)$ bright at the jet base and scattered near-source emission. The northern lobe extends beyond the $^{12}\text{CO}(2 - 1)$ and $\text{SiO}(5 - 4)$ detections (Figure A1), implying a longer dynamical age. Both of these emission features exhibit similar velocity extent (velocity offset from -50 to $+50$ km s $^{-1}$) and comparable collimated spatial morphology (Dutta et al. 2024). The lobe is also traced by $\text{H}_2\text{CO} 3(0, 3) - 2(0, 2)$, which shows knots in the high-resolution map (Figure 4). Fainter emission from $\text{H}_2\text{CO} 3(2, 2) - 2(2, 1)$ is also detected, appearing as a diffuse envelope around the source.

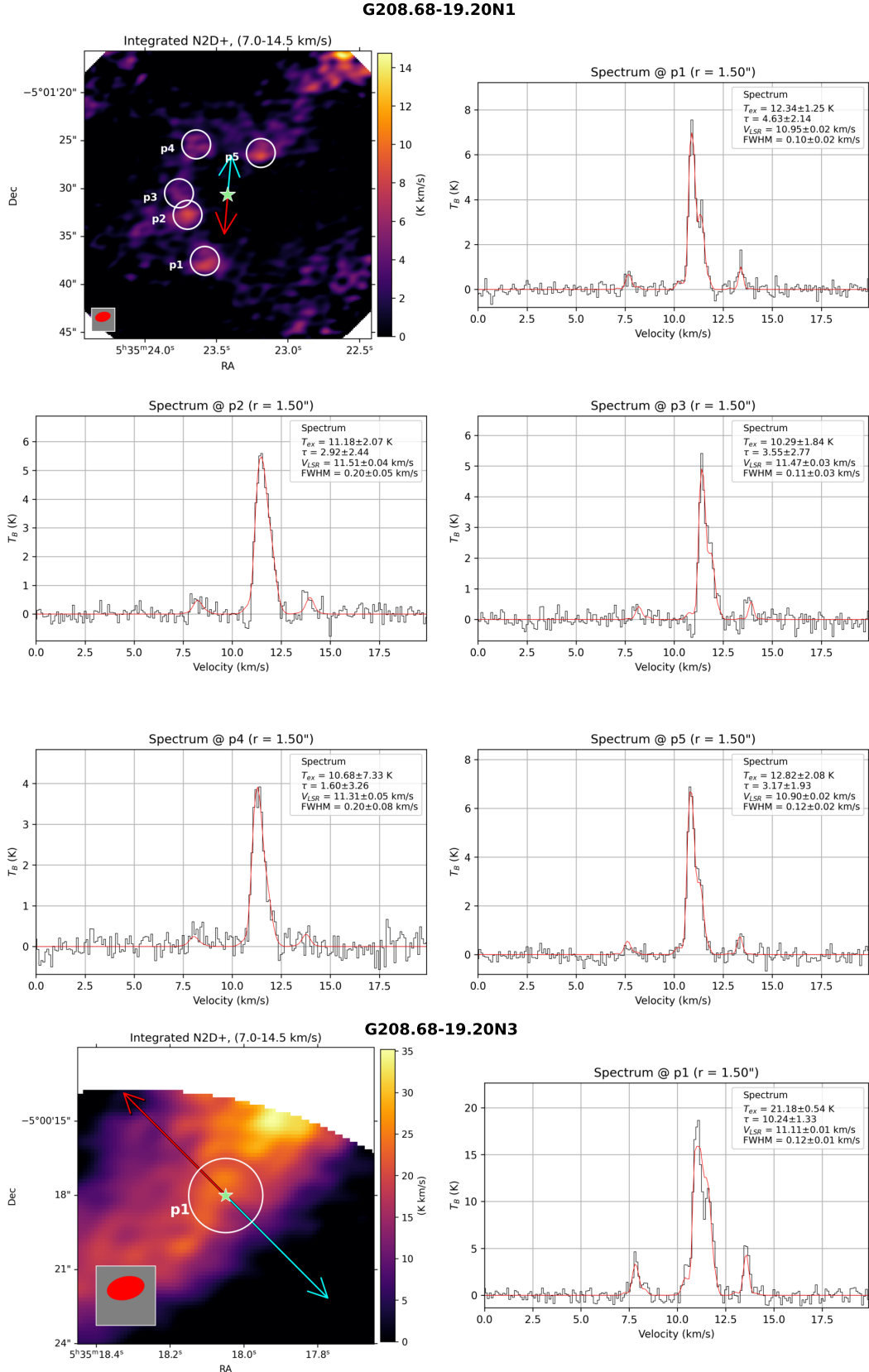


Figure 3. N_2D^+ observed spectra (black) and corresponding model fits (red) for G208.68–19.20N1 and G208.68–19.20N3. Spectra are averaged over apertures with a radius of $1''.5$, centered on positions p1, p2, ... as marked in the integrated maps (color images in the first panel of each object). The derived parameters T_{ex} , τ , V_{LSR} , and V_{FWHM} are indicated within each panel. The continuum peak is marked with an asterisk, and the jet axes follow the orientation shown in Figure A1.

$2(2, 1)$ and $\text{H}_2\text{CO } 3(2, 1) - 2(2, 0)$ is detected along the lobe. Unlike N_2D^+ emission (Section 3.2), H_2CO is mostly observed along the jet axis. Even near the source, within the inner envelope, it likely traces the base of the jet. The peak velocities range from $11\text{--}13 \text{ km s}^{-1}$, although the emission extends from 0 to 22 km s^{-1} , with a FWHM of $5 \pm 2 \text{ km s}^{-1}$.

G208N3 (second row of Figure 4) shows that all four tracers peak at the tip of the northwest lobe, with weaker emission near the continuum. The morphology matches that of CO (2–1) and SiO (5–4) (Figure A1), and the compact extent indicates a short dynamical timescale. Comparable velocity extents (velocity offset from -66 to $+58 \text{ km s}^{-1}$) and similar spatial morphology are observed for both CO and SiO emission (Dutta et al. 2024).

G215M (third row of Figure 4) shows that $\text{CH}_3\text{OH} (4_2 - 3_1)$ traces knots in both lobes, while $\text{H}_2\text{CO } 3(0, 3) - 2(0, 2)$ highlights both knots and diffuse emission across the outflow. The higher H_2CO transitions show a similar distribution to $\text{CH}_3\text{OH} (4_2 - 3_1)$, and the overall morphology agrees with CO (2–1) and SiO (5–4). Similar to G208N1 and G208N3, both CO and SiO emission features exhibit comparable extents (velocity offsets from -40 to $+38 \text{ km s}^{-1}$) and collimated spatial morphology (Dutta et al. 2024).

3.3.1. Rotational Temperatures

We have taken advantage of having three observed transitions of H_2CO to derive the rotational temperatures. As discussed earlier, the H_2CO morphology indicates that these lines could be tracing lower-density outflow material, higher-density knots, or may include contributions from envelope emission at the jet base. To determine the rotational temperatures, we measured the average intensities within a radius of $0''.5$ around the peak position from the high-resolution ($\sim 150 \text{ AU}$) maps integrated over the emitting velocity range. The centers of the selected regions corresponding to the knot peak positions of high-resolution maps are marked in second column of Figure 4 (labeled N01, N02, ..., S01, S02). The rotational diagrams for these regions are presented in Figure 5, where each panel header indicates the corresponding region (N01, N02, ..., S01, S02). These peaks positions are likely jet “knots”. The aperture radius ensures that at least one synthesized beam is included. The Einstein coefficients (A_{ul}) and upper-level energies (E_u) were adopted from the Splatalogue database², as listed in Table 2.

Assuming optically thin emission under local thermodynamic equilibrium (LTE) conditions, the column densities per statistical weight (N_u^{thin}/g_u) are shown in Figure 5 as a function of the upper energy level (E_u) of the lines. The column density of the upper level is given by

$$N_u^{\text{thin}} = \frac{8\pi k\nu^2}{hc^3 A_{ul}} I, \quad (4)$$

where the integrated line intensity is $I = \int T_B dv$, with T_B being the brightness temperature. The best-fit rotational temperatures are indicated in each panel of Figure 5 and in Table 5. Assuming these rotational temperatures to be representative of the excitation temperature of the jet/outflow, we have estimated the total column density, $N_{\text{H}_2\text{CO}}^{\text{tot}}$. The 40% flux uncertainty was adopted as a conservative estimate to account for additional sources of error beyond the nominal ALMA calibration uncertainty ($\sim 10\%$), and typically flux uncertainty 10–20% for most ALMA datasets. In our case, the spectra were extracted from relatively extended and scattered-intensity emission regions in a few cases (see Figure 4), where uncertainties from baseline subtraction and missing short-spacing flux can contribute significantly. To avoid underestimating the propagated uncertainties in the derived quantities, such as rotational temperatures and column densities, we therefore adopted a total flux uncertainty of 40%. The quoted errors on T_{rot} and N_{tot} are therefore the formal fitting errors derived from the covariance matrix of the weighted linear regression, given the assumed flux uncertainties.

The slopes of the emission near the continuum peak of G208N1 (positions N01 and S01) deviate from the expected trend in the rotation diagram, yielding unphysical (negative) temperature estimates; these values are therefore excluded. The anomalous slopes are likely due to optical depth effects, as the lower transition $\text{H}_2\text{CO } 3(0, 3) - 2(0, 2)$ appears optically thick near the source. Likewise, the $\text{H}_2\text{CO } 3(2, 2) - 2(2, 1)$ and $\text{H}_2\text{CO } 3(2, 1) - 2(2, 0)$ emission at position S01 of G215M is weak or undetected and may be affected by optical depth, resulting in large uncertainties in the rotational temperature fitting (Table 5).

3.3.2. H_2CO Non-LTE Analyses

To investigate the opacity levels, we estimated the line opacities in the regions described above using a non-LTE radiative transfer approach. We employed the RADEX code (van der Tak et al. 2007), following the methodology of Hsieh et al. (2015), which utilizes an opacity-weighted radiation temperature to characterize the molecular excitation.

RADEX computes the level populations of H_2CO by solving the statistical equilibrium equations, accounting

² <https://splatalogue.online/>

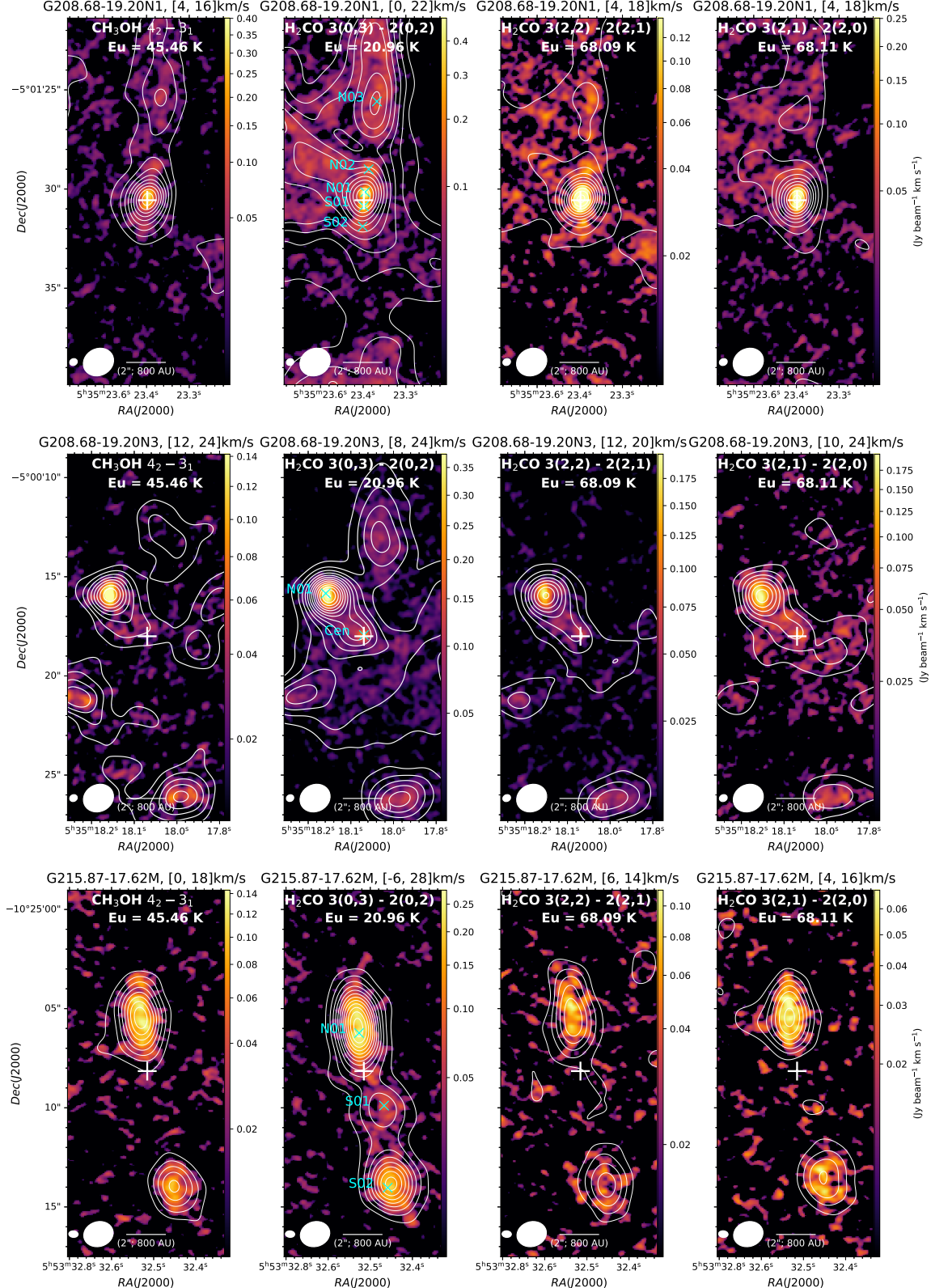


Figure 4. High-resolution (~ 150 AU) emission maps integrated over the velocity ranges indicated in each panel of CH_3OH ($4_2 - 3_1$) (column 1), $\text{H}_2\text{CO } 3(0,3) - 2(0,2)$ (column 2), $\text{H}_2\text{CO } 3(2,2) - 2(2,1)$ (column 3), and $\text{H}_2\text{CO } 3(2,1) - 2(2,0)$ (column 4). Rows 1, 2, and 3 correspond to the sources G208N1, G208N3, and G215M, respectively. White contours show low-resolution (~ 500 AU) taper maps integrated over the same velocity ranges, taken from Figure A2, with contour levels starting at 3σ and increasing in steps of 3σ . The σ values (in $\text{mJy beam}^{-1} \text{ km s}^{-1}$) for each molecule and source are: G208N1 (0.030, 0.052, 0.035, 0.035), G208N3 (0.020, 0.045, 0.025, 0.025), and G215M (0.025, 0.035, 0.016, 0.016). The continuum peak is marked with a white plus (+). Approximate knot centers are labeled N01, N02, ... in the northern lobe and S01, S02, ... in the southern lobe.

for both collisional and radiative processes. This non-LTE treatment is essential in environments where the local density is insufficient to thermalize the molecular levels. The code applies an escape-probability formalism to approximate photon trapping, providing realistic estimates of line opacities without assuming LTE conditions.

From our analysis, we find that the lower transitions of H₂CO (H₂CO 3(0, 3) – 2(0, 2) and H₂CO 3(2, 2) – 2(2, 1)) exhibit opacities of $\tau_\nu > 1.0$ in the N01 and S01 regions of G208N1, confirming that these transitions are optically thick, while the higher transition H₂CO 3(2, 1) – 2(2, 0) shows $\tau_\nu < 1.0$, indicating optically thin emission. This optical thickness explains the opposite slopes observed in Figure 5 (N01 and S01). The estimated fluxes of lower transitions in these regions represent lower limits, and the derived temperatures should therefore be regarded as upper limits. In contrast, all other regions in G208N1, G208N3, and G215M show $\tau_\nu < 1.0$, supporting the assumption of optically thin emission.

Table 5. Rotational temperatures and column densities of H₂CO for each peak in Figure 4

Region	T_{rot} (K)	N_{tot} (e+14 cm ⁻²)
G208N1		
N03	75.1 ± 67.8	2.83 ± 1.94
N02	163.6 ± 88.7	2.77 ± 0.52
N01	--	--
S01	--	--
S02	128.4 ± 55.9	2.51 ± 0.48
G208N3		
N01	191.4 ± 94.0	6.73 ± 0.98
Cen	110.0 ± 37.5	3.00 ± 0.53
G215M		
N01	53.5 ± 7.2	5.39 ± 0.77
S01	27.7 ± 27.5	2.05 ± 4.18
S02	49.6 ± 10.6	4.19 ± 1.02

4. DISCUSSION

The key observational results—including detections of multiple molecular species at a common angular resolution, their projected sizes, signatures of sublimation and depletion, and rotational temperatures measured along the jets—are summarized in Figure 6 and Table 1. These diagnostics collectively provide insight into the physical conditions and evolutionary stages of the protostellar cores.

4.1. Local Gas Heating by the Protostars

Radiation from the central protostar heats the surrounding medium. As the protostar evolves, its temperature and luminosity vary in response to both accretion and internal evolution, driving changes in the thermal and chemical structure of the envelope.

G208N1, previously classified as a hot corino (Hsu et al. 2020, 2022), shows signatures of advanced chemical processing. The higher temperature in its inner envelope likely destroys N₂D⁺ via reactions with CO, producing DCO⁺. Consequently, N₂D⁺ is depleted near the continuum peak, forming an extended arc-like shell, while C¹⁸O emission appears relatively faint. Its luminosity exceeds that of several benchmark Class 0 sources e.g., HH 211, HH 111, B335 (Lee 2020; Dutta et al. 2024), possibly due to a recent accretion burst in this source. Such a burst would shift the CO snowline outward and give rise to the large N₂D⁺ shell surrounding the source. Notably, N₂D⁺ exhibits excitation temperatures of $\sim 10\text{--}13$ K in that ring (section 3.2). The detection of compact CH₃OH (10₂ – 9₃) emission around the continuum peak and its absence across the extended envelope and the weak C¹⁸O emission around the extended envelope are consistent with earlier findings (Hsu et al. 2024). These features likely result from freeze-out of CO and CH₃OH onto dust grains in the cold, dense outer envelope. Methanol is only released into the gas phase in the warm inner region near the protostar. The enhanced DCO⁺ toward the center implies that H₂D⁺ may still persist in this region. Detection of DCN further indicates a warm environment, since it is formed both via warm channels involving CH₂D⁺ ($\sim 62\%$) and cold channels involving H₂D⁺ ($\sim 22\%$) (Turner 2001).

H₂CO emission is primarily associated with the jet and outflows, as indicated by its absence in the inner core and its alignment along the outflow axis. Two bright knots near the jet base (Figure 4) suggest localized heating. H₂CO can form through gas-phase reactions (e.g., CH₂ + O, CH₃ + O) (Yamamoto 2017) or by CO hydrogenation on dust grains, followed by thermal desorption above ~ 40 K (Garrod & Herbst 2006). The observed rotational diagrams for N01 and S01 region (Figure 5) indicate optical depth effects in the lower transitions (section 3.3.2). The detection of both C¹⁸O and CH₃OH near the jet base supports their efficient release through sublimation, followed by subsequent gas-phase chemistry leading to the formation of H₂CO.

For G208N3, the envelope traced by N₂D⁺ and DCO⁺ is filamentary, while the core remains relatively compact in DCO⁺. Interestingly, N₂D⁺ exhibits excitation temperatures of $\sim 21.18 \pm 0.54$ K around the protostar G208N3, which is significantly higher than that in ring like structure in G208N1 (section 3.2). Detection of

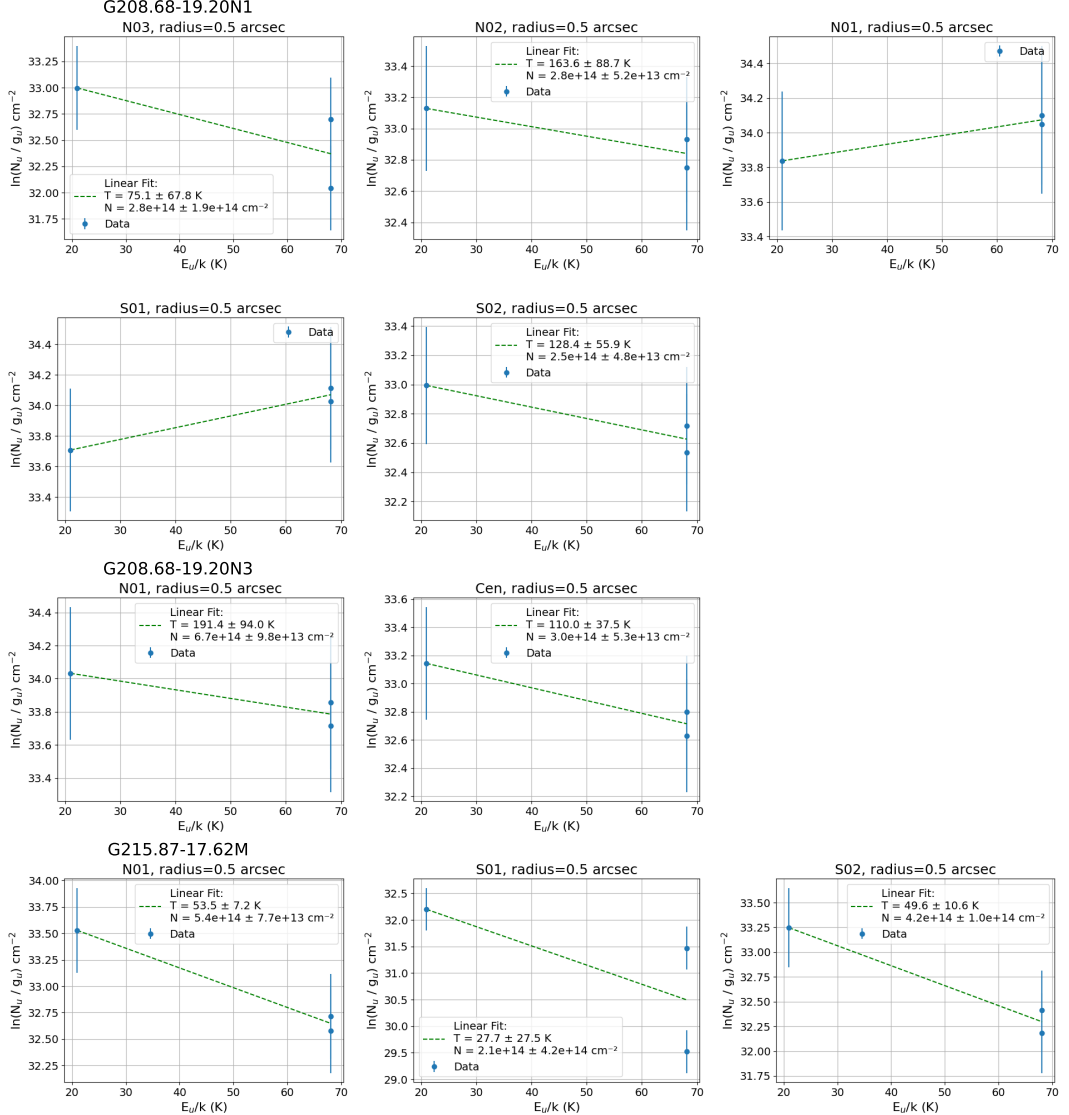


Figure 5. Rotation diagrams for the molecular transitions of H₂CO are shown for three different objects. These diagrams are derived from the average intensities within 0''.5 along the outflow/jet axis, indicated by cross marks in Figure 4. The same regions around the knots, marked with circles, are labeled as N1, N2, ..., Cent, S1, S2. Error bars represent the assumed conservative uncertainties in our measurements, approximately 40% of the estimated values. The green solid lines show linear fits to the observed data points. The rotational temperatures and column densities derived from these fits are displayed in the corresponding panels.

DCN and DCO⁺ implies a moderately warm environment, though the weak C¹⁸O and H₂CO suggest conditions close to the CO sublimation threshold.

In G215M, high-resolution maps reveal compact C¹⁸O emission confined to the continuum peak, while low-resolution maps show no extended component. N₂D⁺ and DCO⁺ are weak and irregular, and DCN is absent. These signatures suggest a colder environment with inefficient synthesis of CO-derived species.

We note that the hyperfine temperatures derived from N₂D⁺ (Table 4) are significantly lower than the rota-

tional temperatures estimated from the H₂CO transitions (Table 5). The N₂D⁺ emission primarily traces cooler regions, mostly associated with the surrounding envelope, whereas the H₂CO transitions probe more excited regions in the jets or at the jet base within the envelope. Consequently, the H₂CO temperatures are naturally higher.

In summary, the relative sizes of C¹⁸O emission, depletion of N₂D⁺, and presence of CO-derived molecules (DCO⁺, DCN) collectively trace the evolutionary progression. G208N1 shows the most advanced chemistry

and heating, G208N3 represents an intermediate stage, and G215M is likely the youngest source.

4.2. Status of the Outflow Emission

In G208N1, the SiO and CO morphology (Figure A1) and position–velocity diagrams (Dutta et al. 2024) show nearly identical velocity dispersions, complicating separation of outflow and jet components. The system shows a collimated jet with mean deprojected velocities $V_j \sim 102^{+24}_{-35} \text{ km s}^{-1}$ and a high mass-loss rate of $\dot{M}_j \sim 2.5 \times 10^{-6} M_\odot \text{ yr}^{-1}$. The dynamical age is constrained to $\mathcal{T}_{\text{dyn}} \sim 47^{+38}_{-10} \text{ yr}$ based on compact SiO and CO emission, though the northern lobe likely extends farther, yielding a conservative estimate of $\sim 1000 \text{ yr}$. H₂CO emission yields $T_{\text{rot}} \sim 75\text{--}164 \text{ K}$ and $N_{\text{tot}} \sim (2.51\text{--}2.83) \times 10^{14} \text{ cm}^{-2}$ in the knots (Figure 4; Table 5). Strong CH₃OH transitions further support high kinetic temperatures, consistent with CO sublimation and subsequent molecule formation along the jet.

For G208N3, SiO and CO exhibit similar velocity dispersions, again making it difficult to separate jet from outflow. The kinematics suggest a young jet launched only a few hundred years ago, with a blue lobe dynamical age of $\mathcal{T}_{\text{dyn}} \sim 228^{+160}_{-110} \text{ yr}$. The deprojected velocity is $V_j \sim 61^{+41}_{-15} \text{ km s}^{-1}$, and the mass-loss rate is $\dot{M}_j \sim 1.3 \times 10^{-6} M_\odot \text{ yr}^{-1}$ (Table 1). H₂CO shows high $T_{\text{rot}} \sim 110\text{--}193 \text{ K}$ and $N_{\text{tot}} \sim (3.0\text{--}6.7) \times 10^{14} \text{ cm}^{-2}$ in the outer knots, accompanied by CH₃OH emission with a similar spatial distribution. These results suggest that shock heating within the jet is sufficient to sublimate CO and form complex molecules, with minimal influence from protostellar UV radiation.

In case of G215M, SiO and CO exhibit similar velocity structures, with a mean deprojected velocity of $V_j \sim 60^{+28}_{-13} \text{ km s}^{-1}$ and a mass-loss rate of $\dot{M}_j \sim 0.32 \times 10^{-6} M_\odot \text{ yr}^{-1}$. The estimated dynamical age is $\mathcal{T}_{\text{dyn}} \sim 292^{+133}_{-108} \text{ yr}$ (Table 1). The outflow chemistry indicates cooler conditions, with H₂CO rotational temperatures of only $T_{\text{rot}} \sim 50\text{--}54 \text{ K}$ and column densities $N_{\text{tot}} \sim (4.2\text{--}5.4) \times 10^{14} \text{ cm}^{-2}$, excluding the estimation at S01 with high errorbars. CH₃OH emission is weak and co-spatial with H₂CO, implying limited CO sublimation.

4.3. Evolutionary status of the Protostars

G208N1 is a luminous Class 0 protostar with a massive envelope and extended size of 4000–5000 AU (Table 1). Its very high luminosity indicates a recent outburst, which is supported by the N₂D⁺ cavity in the continuum peak and semi-arc like structure surrounding the continuum. Its powerful, collimated jet exhibits high velocities and a large mass-loss rate, with a dynamical

age possibly ranging from a few decades to $\sim 10^3 \text{ yr}$. Slightly elevated rotational temperatures of H₂CO and strong CH₃OH emission indicate efficient heating and CO sublimation along the jet, consistent with chemical enrichment driven by shocks. Together, these characteristics identify G208N1 as an energetic young protostar undergoing active accretion and feedback.

In contrast to G208N1, G208N3 is less luminous and more poorly characterized, with a smaller envelope mass and smaller envelope size (1200–2000AU; Table 1). Its jet is younger and slower, a mass-loss rate about half that of G208N1, and a dynamical age of only a few hundred years. Despite its lower energetics, H₂CO and CH₃OH indicate similarly high rotational temperatures, consistent with shock heating and CO sublimation along the jet. These results suggest that while G208N3 drives a weaker and younger outflow than G208N1, the chemical enrichment processes in the jet are broadly comparable.

Compared to G208N1 and G208N3, G215M is less massive and less chemically evolved. With an envelope mass of only $\sim 0.3 M_\odot$ and smaller size (1000–2400 AU; Table 1), it drives a slower and weaker jet with a dynamical age of a few hundred years. Unlike the hotter conditions in G208N1 and G208N3, the H₂CO rotational temperatures in G215M are relatively low, and CH₃OH emission is weak, suggesting limited CO sublimation and less efficient shock chemistry. These properties indicate that G215M is likely forming a low-mass star with reduced accretion and feedback, representing an earlier and less chemically enriched stage compared to the other two sources.

It is important to note that the different morphologies of the species may arise from varying physical conditions, rather than being solely determined by protostellar evolution. For instance, if a source is in a quiescent accretion phase and thus has a low luminosity—as might be the case for G208N3 and G215M—the region where CO is not depleted would remain small, even if the source is relatively evolved. At the current angular resolution, such a compact region may not be detectable, which could lead to the source being misclassified as less evolved.

4.4. Comparison with Previous Studies of Low-Mass Protostars

Several previous studies have demonstrated that molecular tracers provide powerful diagnostics of the thermal and chemical structure in deeply embedded protostars. Formaldehyde has long been used as a probe of gas temperatures in envelopes and outflows; for example, Maret et al. (2004) and Jørgensen et al. (2005)

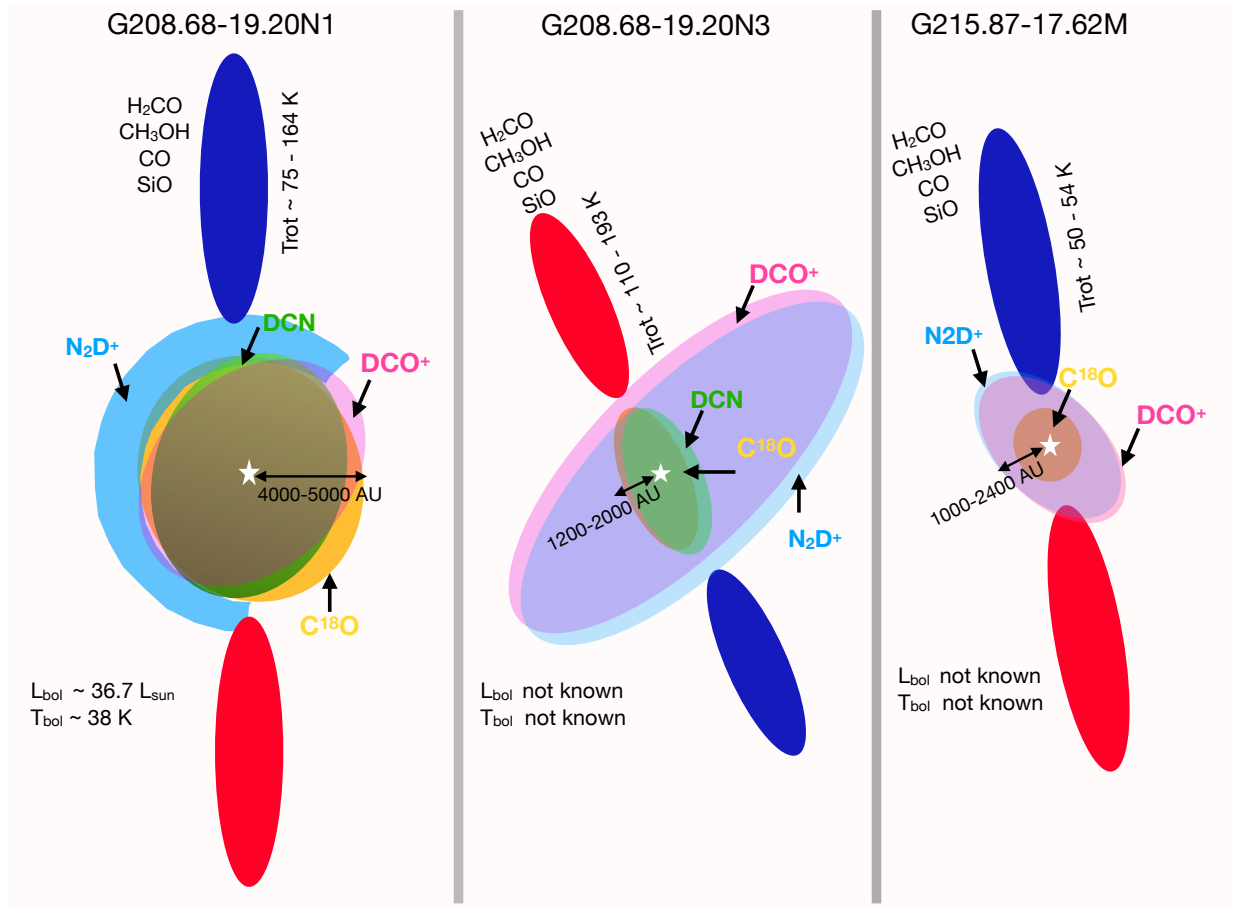


Figure 6. Cartoon summary of detected species for the three protostars. Molecular species are shown in distinct colors, scaled relative to their observed extents. Continuum peaks are marked by stars.

showed that multi-transition H₂CO observations of envelopes in Class 0 sources at low-resolution using JCMT and IRAM telescope reveal abundance jumps when dust goes beyond grain evaporation limit, ~ 100 K. Deuterated species, in contrast, are more sensitive to colder conditions. Surveys of N₂D⁺ and deuterated formaldehyde toward young cores (Roberts & Millar 2007; Emprichtinger et al. 2009) established that high deuteration fractions trace CO-depleted envelopes and decline with protostellar heating, making them robust evolutionary indicators.

High-resolution ALMA observations have since confirmed and extended this picture across several well-studied low-mass protostars. In the binary system IRAS 16293–2422, Persson et al. (2018) found H₂CO excitation temperatures of ~ 100 K in the inner envelope, and formaldehyde forms in the ice as soon as CO has frozen onto the grains. In IRAS 15398–3359, Okuda et al. (2020) showed that higher-energy H₂CO transitions are compact and warm near the source, whereas lower-energy lines are extended along the outflow, yielding excitation temperatures of 40–60 K in shocked re-

gions. Observations of VLA 1623–2417 as part of the FAUST program (Mercimek et al. 2025) revealed strong spatial differentiation: hot-corino gas at ~ 125 K, outflow cavities at 20–40 K, and cold streamers at ≤ 15 K with the highest deuteration levels. For L1551 IRS5, Bianchi et al. (2020) reported a hot corino around the protostellar binary with methanol and complex organics peaking at ~ 100 K, confirming the existence of warm inner envelopes. More recently, FAUST observations of NGC 1333 IRAS 4A2 (Frediani et al. 2025) revealed compact CH₃OH and iCOM emission within 20–50 au, consistent with hot-corino chemistry, while radial temperature profiling demonstrated chemical segregation in the warm inner envelope.

Together, these case studies highlight a consistent trend: in our targets, H₂CO transitions predominantly trace warm, shocked, or jet-base gas, while N₂D⁺ and other deuterated tracers probe the colder envelope. We note, however, that H₂CO emission can also arise in a wider range of environments, including outflow cavities or streamers at lower temperatures (< 20 K), as reported in studies of low-mass protostars. In our

sources (G208N1, G208N3, and G215M), the elevated H₂CO excitation temperatures and spatial association with jet-like features suggest that the observed emission mainly traces warm, possibly shock-heated gas. This tracer-dependent thermal differentiation provides a robust framework for assessing the evolutionary stages of young protostars and situates our Orion sources within the broader context of well-studied low-mass systems.

5. SUMMARY AND CONCLUSION

We have studied the inner envelopes of three protostellar cores to investigate the evolutionary structures at the very early stage of star formation. Based on the depletion and sublimation of various molecular species, their emitting sizes around the core, the outflow characteristics, we have drawn an evolutionary status of these three sources.

(i) G208N1 envelope is detected with bright C¹⁸O, N₂D⁺ cavity, DCN, DCO⁺, CH₃OH(10₂ – 9₃), CH₃OH(4₂ – 3₁), H₂CO. The jet base and extended outflow emission are detected with CH₃OH(4₂ – 3₁) and H₂CO transitions.

(ii) G208N3 envelope is detected with scattered extended C¹⁸O, within filamentary N₂D⁺ and DCO⁺, extended DCN and H₂CO transitions. The outflow emission is detected with CH₃OH(4₂ – 3₁) and H₂CO transitions.

(iii) G215M is detected with compact C¹⁸O, scattered and weak N₂D⁺ and DCO⁺, extended DCN. The extended outflow emission is detected with CH₃OH(4₂ – 3₁) and H₂CO transitions.

(iv) The H₂CO rotational temperatures were estimated in the knots of the extended outflows for all three sources. Among them, G208N3 exhibits the highest T_{rot} values, while G215M shows the lowest.

Based on their chemical compositions, sizes, envelope sublimation and depletion, continuum masses, and jet physical properties, it is evident that G208N1 (HOPS 87) is the most actively accreting and is likely the most evolved among the three protostars. G208N3 and G215M show weaker accretion activity; G208N3 may be younger than G208N1, whereas G215M is probably the youngest source. Variability in luminosity or accretion state could also influence their chemical mor-

phologies. High-resolution studies to determine the protostellar central masses from envelope kinematics, along with sensitive multiwavelength observations to construct spectral energy distributions (SEDs), will help clarify the evolutionary distinctions among these sources. Expanding such chemical analyses to a larger sample of very young protostars will be crucial for statistically establishing chemical and morphological trends as diagnostic tools for understanding the earliest stages of protostellar evolution.

6. ACKNOWLEDGMENTS

We are thankful to the anonymous reviewer for their valuable suggestions, which helped to improve the overall quality of this paper. We are thankful to Tien-Hao Hsieh for discussion at various stages. This paper makes use of the following ALMA data: ADS/JAO.ALMA#2018.1.00302.S. ALMA is a partnership of ESO (representing its member states), NSF (USA) and NINS (Japan), together with NRC (Canada), NSC and ASIAA (Taiwan), and KASI (Republic of Korea), in cooperation with the Republic of Chile. The Joint ALMA Observatory is operated by ESO, AUI/NRAO and NAOJ. C.-F.L. acknowledges the grant from the National Science and Technology Council of Taiwan (112-2112-M-001-039-MY3). This research is sponsored by NSTC 113-2124-M-001-008- and NSTC 114-2124-M-001-015-. D.J. is supported by NRC Canada and by an NSERC Discovery Grant. MJ acknowledges the support of the Research Council of Finland Grant No. 348342. S.-Y.H. acknowledges support from the Academia Sinica of Taiwan (grant No. AS-PD-1142-M02-2).

Facility: ALMA

Software: Astropy (Astropy Collaboration et al. 2013, 2018), APLpy (Robitaille & Bressert 2012), Matplotlib (Hunter 2007), CASA (McMullin et al. 2007), pyspeckit (Ginsburg et al. 2022) .

APPENDIX

A. OUTFLOW AND JETS

SiO and CO emissions of G208N1, G208N3, and G215M are shown in Figure A1 at a resolution of \sim 150 AU. In all cases, the emission traces narrow, collimated jets. We define the jet/outflow axis position angle (PA) as the angle measured east of north, with north at 0° and east at 90°. A single PA in the range 0° to 180° is reported, corresponding

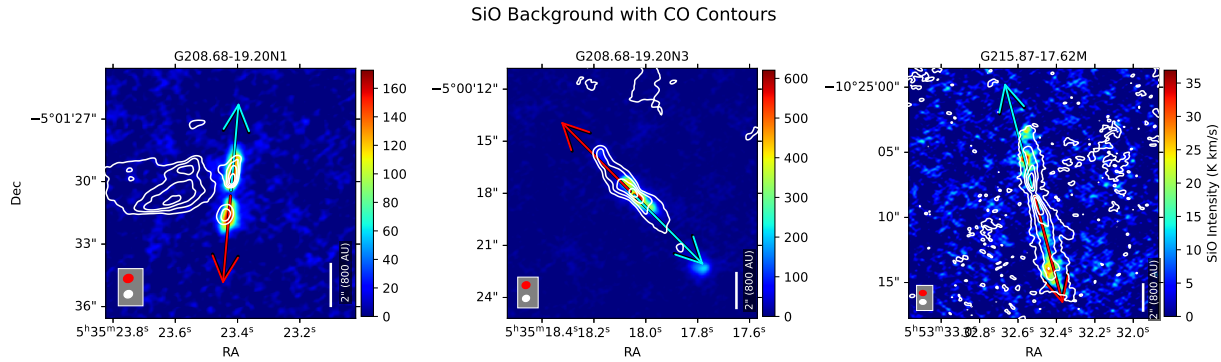


Figure A1. This image, reproduced following Dutta et al. (2024), illustrates the jet axis and compares the CO and SiO emission with the other molecular tracers presented in this study. SiO emission is shown in the background, with CO emission overlaid as contours. The contour levels span from the 95th percentile value of the CO data up to its maximum, divided into five intervals. Beam sizes are indicated in the lower left corner, SiO in red and CO in white. The blue- and red-shifted jet axes are marked with cyan and red arrows, respectively.

to the direction of the blue-shifted lobe modulo 180° . For example, in G208.68–19.20N1, the blue-shifted lobe has a PA of approximately 355° , which corresponds to an outflow axis PA of $\sim 175^\circ$. Similarly, the jets of G208N3 and G215M have PAs of $\sim 45^\circ$ and $\sim 15^\circ$, respectively.

CH_3OH and H_2CO Emission along jet axis at low resolution (~ 500 AU) are shown in Figure A2.

REFERENCES

Arce, H. G., Shepherd, D., Gueth, F., et al. 2007, in Protostars and Planets V, ed. B. Reipurth, D. Jewitt, & K. Keil, 245, doi: [10.48550/arXiv.astro-ph/0603071](https://arxiv.org/abs/0603071)

Astropy Collaboration, Robitaille, T. P., Tollerud, E. J., et al. 2013, *A&A*, 558, A33, doi: [10.1051/0004-6361/201322068](https://doi.org/10.1051/0004-6361/201322068)

Astropy Collaboration, Price-Whelan, A. M., Sipőcz, B. M., et al. 2018, *AJ*, 156, 123, doi: [10.3847/1538-3881/aabc4f](https://doi.org/10.3847/1538-3881/aabc4f)

Bally, J. 2016, *ARA&A*, 54, 491, doi: [10.1146/annurev-astro-081915-023341](https://doi.org/10.1146/annurev-astro-081915-023341)

Bianchi, E., Chandler, C. J., Ceccarelli, C., et al. 2020, *MNRAS*, 498, L87, doi: [10.1093/mnrasl/slaa130](https://doi.org/10.1093/mnrasl/slaa130)

Bontemps, S., Andre, P., Terebey, S., & Cabrit, S. 1996, *A&A*, 311, 858

Caselli, P., Walmsley, C. M., Tafalla, M., Dore, L., & Myers, P. C. 1999, *ApJL*, 523, L165, doi: [10.1086/312280](https://doi.org/10.1086/312280)

Dutta, S., Lee, C.-F., Liu, T., et al. 2020, *ApJS*, 251, 20, doi: [10.3847/1538-4365/abba26](https://doi.org/10.3847/1538-4365/abba26)

Dutta, S., Lee, C.-F., Johnstone, D., et al. 2024, *AJ*, 167, 72, doi: [10.3847/1538-3881/ad152b](https://doi.org/10.3847/1538-3881/ad152b)

Emprichtinger, M., Caselli, P., Volgenau, N. H., Stutzki, J., & Wiedner, M. C. 2009, *A&A*, 493, 89, doi: [10.1051/0004-6361:200810324](https://doi.org/10.1051/0004-6361:200810324)

Endres, C. P., Schlemmer, S., Schilke, P., Stutzki, J., & Müller, H. S. P. 2016, *Journal of Molecular Spectroscopy*, 327, 95, doi: [10.1016/j.jms.2016.03.005](https://doi.org/10.1016/j.jms.2016.03.005)

Flower, D. R., Pineau Des Forêts, G., & Walmsley, C. M. 2006, *A&A*, 449, 621, doi: [10.1051/0004-6361:20054246](https://doi.org/10.1051/0004-6361:20054246)

Frank, A., Ray, T. P., Cabrit, S., et al. 2014, in Protostars and Planets VI, ed. H. Beuther, R. S. Klessen, C. P. Dullemond, & T. Henning, 451–474, doi: [10.2458/azu_uapress_9780816531240-ch020](https://doi.org/10.2458/azu_uapress_9780816531240-ch020)

Frediani, J., De Simone, M., Testi, L., et al. 2025, *A&A*, 695, A78, doi: [10.1051/0004-6361/202452191](https://doi.org/10.1051/0004-6361/202452191)

Furlan, E., Fischer, W. J., Ali, B., et al. 2016, *ApJS*, 224, 5, doi: [10.3847/0067-0049/224/1/5](https://doi.org/10.3847/0067-0049/224/1/5)

Garrod, R. T., & Herbst, E. 2006, *A&A*, 457, 927, doi: [10.1051/0004-6361:20065560](https://doi.org/10.1051/0004-6361:20065560)

Ginsburg, A., Sokolov, V., de Val-Borro, M., et al. 2022, *AJ*, 163, 291, doi: [10.3847/1538-3881/ac695a](https://doi.org/10.3847/1538-3881/ac695a)

Hirano, N., Sahu, D., Liu, S.-Y., et al. 2024, *ApJ*, 961, 123, doi: [10.3847/1538-4357/ad09e2](https://doi.org/10.3847/1538-4357/ad09e2)

Hsieh, T.-H., Lai, S.-P., Belloche, A., Wyrowski, F., & Hung, C.-L. 2015, *ApJ*, 802, 126, doi: [10.1088/0004-637X/802/2/126](https://doi.org/10.1088/0004-637X/802/2/126)

Hsu, S.-Y., Liu, S.-Y., Liu, T., et al. 2020, *ApJ*, 898, 107, doi: [10.3847/1538-4357/ab9f3a](https://doi.org/10.3847/1538-4357/ab9f3a)

—. 2022, *ApJ*, 927, 218, doi: [10.3847/1538-4357/ac49e0](https://doi.org/10.3847/1538-4357/ac49e0)

Hsu, S.-Y., Lee, C.-F., Liu, S.-Y., et al. 2024, *ApJ*, 976, 29, doi: [10.3847/1538-4357/ad7e25](https://doi.org/10.3847/1538-4357/ad7e25)

Hunter, J. D. 2007, *Computing in Science and Engineering*, 9, 90, doi: [10.1109/MCSE.2007.55](https://doi.org/10.1109/MCSE.2007.55)

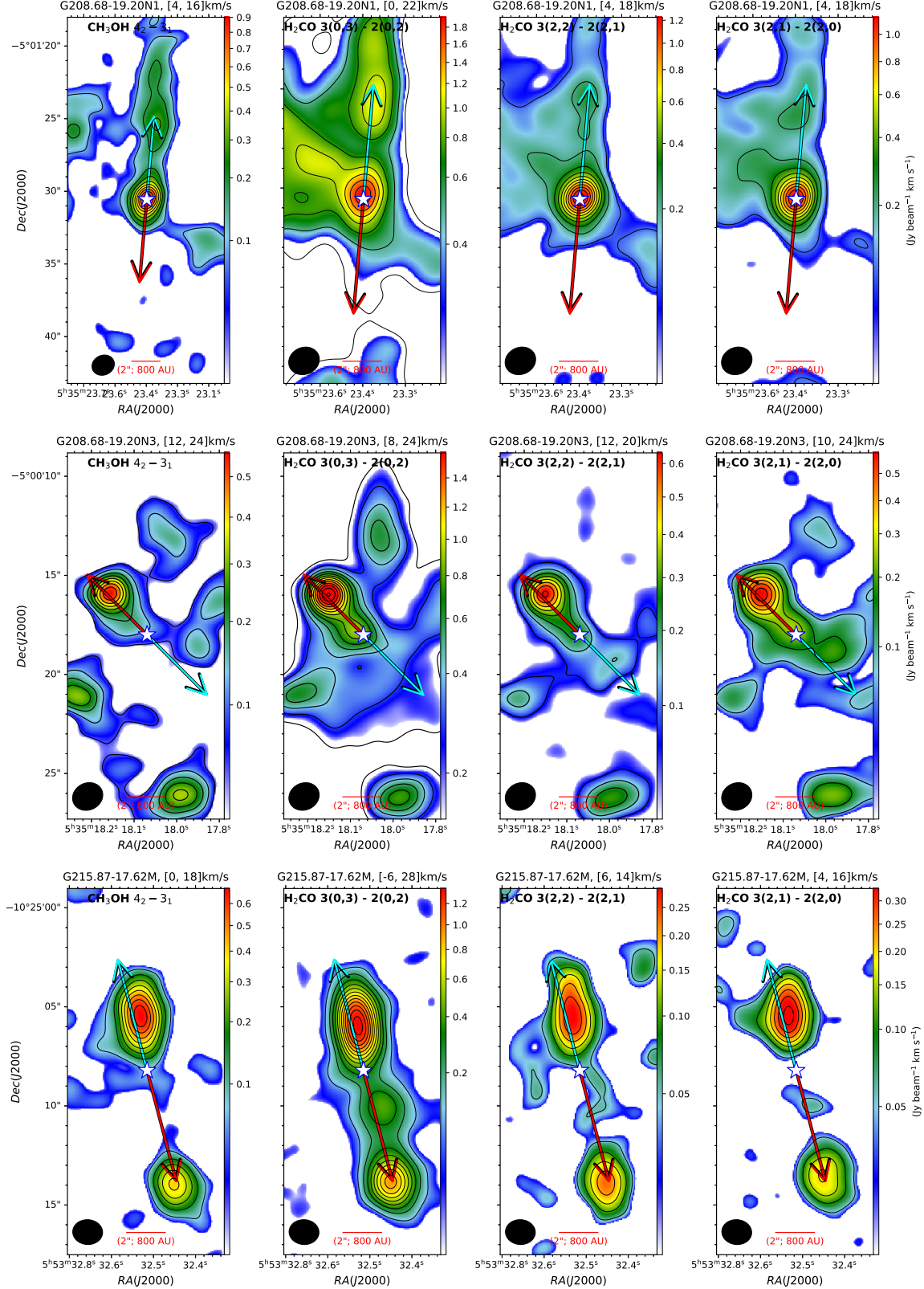


Figure A2. Low-resolution UV-tapered (~ 500 AU) emission maps, integrated over the velocity ranges indicated in each panel, are shown for CH₃OH (4₂ – 3₁) (column 1), H₂CO 3(0, 3) – 2(0, 2) (column 2), H₂CO 3(2, 2) – 2(2, 1) (column 3), and H₂CO 3(2, 1) – 2(2, 0) (column 4). Rows correspond to the sources G208N1, G208N3, and G215M, respectively. Contours start at 3σ and increase in steps of 3σ , where σ (in mJy beam $^{-1}$ km s $^{-1}$) is: G208N1 — (0.030, 0.052, 0.035, 0.035); G208N3 — (0.020, 0.045, 0.025, 0.025); G215M — (0.025, 0.035, 0.016, 0.016). The continuum peak is marked with an asterisk, while blueshifted and redshifted jet axes are indicated by cyan and red arrows, respectively. Scalebars are shown, and beam sizes are indicated in the lower-left corner of each panel.

Jansen, D. J., Spaans, M., Hogerheijde, M. R., & van Dishoeck, E. F. 1995, *A&A*, 303, 541

Jørgensen, J. K., Schöier, F. L., & van Dishoeck, E. F. 2005, *A&A*, 437, 501, doi: [10.1051/0004-6361:20042060](https://doi.org/10.1051/0004-6361:20042060)

Kim, G., Tatematsu, K., Liu, T., et al. 2020, *ApJS*, 249, 33, doi: [10.3847/1538-4365/aba746](https://doi.org/10.3847/1538-4365/aba746)

Lee, C.-F. 2020, *A&A Rv*, 28, 1, doi: [10.1007/s00159-020-0123-7](https://doi.org/10.1007/s00159-020-0123-7)

Lee, J.-E., Bergin, E. A., & Evans, II, N. J. 2004, *ApJ*, 617, 360, doi: [10.1086/425153](https://doi.org/10.1086/425153)

Li, S., Sanhueza, P., Lu, X., et al. 2022, *ApJ*, 939, 102, doi: [10.3847/1538-4357/ac94d4](https://doi.org/10.3847/1538-4357/ac94d4)

Maret, S., Ceccarelli, C., Caux, E., et al. 2004, *A&A*, 416, 577, doi: [10.1051/0004-6361:20034157](https://doi.org/10.1051/0004-6361:20034157)

McMullin, J. P., Waters, B., Schiebel, D., Young, W., & Golap, K. 2007, in *Astronomical Society of the Pacific Conference Series*, Vol. 376, *Astronomical Data Analysis Software and Systems XVI*, ed. R. A. Shaw, F. Hill, & D. J. Bell, 127

Mercimek, S., Codella, C., Podio, L., et al. 2025, *MNRAS*, 538, 1481, doi: [10.1093/mnras/staf367](https://doi.org/10.1093/mnras/staf367)

Müller, H. S. P., & Lewen, F. 2017, *Journal of Molecular Spectroscopy*, 331, 28, doi: [10.1016/j.jms.2016.10.004](https://doi.org/10.1016/j.jms.2016.10.004)

Müller, H. S. P., Schlöder, F., Stutzki, J., & Winnewisser, G. 2005, *Journal of Molecular Structure*, 742, 215, doi: [10.1016/j.molstruc.2005.01.027](https://doi.org/10.1016/j.molstruc.2005.01.027)

Müller, H. S. P., Thorwirth, S., Roth, D. A., & Winnewisser, G. 2001, *A&A*, 370, L49, doi: [10.1051/0004-6361:20010367](https://doi.org/10.1051/0004-6361:20010367)

Müller, H. S. P., Winnewisser, G., Demaison, J., Perrin, A., & Valentin, A. 2000, *Journal of Molecular Spectroscopy*, 200, 143, doi: [10.1006/jmsp.1999.8027](https://doi.org/10.1006/jmsp.1999.8027)

Okuda, Y., Oya, Y., Sakai, N., Watanabe, Y., & Yamamoto, S. 2020, *ApJ*, 900, 40, doi: [10.3847/1538-4357/aba51e](https://doi.org/10.3847/1538-4357/aba51e)

Parise, B., Leurini, S., Schilke, P., et al. 2009, *A&A*, 508, 737, doi: [10.1051/0004-6361/200912774](https://doi.org/10.1051/0004-6361/200912774)

Persson, M. V., Jørgensen, J. K., Müller, H. S. P., et al. 2018, *A&A*, 610, A54, doi: [10.1051/0004-6361/201731684](https://doi.org/10.1051/0004-6361/201731684)

Reipurth, B., & Bally, J. 2001, *ARA&A*, 39, 403, doi: [10.1146/annurev.astro.39.1.403](https://doi.org/10.1146/annurev.astro.39.1.403)

Roberts, H., & Millar, T. J. 2007, *A&A*, 471, 849, doi: [10.1051/0004-6361:20066608](https://doi.org/10.1051/0004-6361:20066608)

Robitaille, T., & Bressert, E. 2012, *APLpy: Astronomical Plotting Library in Python*, *Astrophysics Source Code Library*, record ascl:1208.017. <http://ascl.net/1208.017>

Sipilä, O., Caselli, P., & Harju, J. 2015, *A&A*, 578, A55, doi: [10.1051/0004-6361/201424364](https://doi.org/10.1051/0004-6361/201424364)

Tobin, J. J., Sheehan, P. D., Megeath, S. T., et al. 2020, *ApJ*, 890, 130, doi: [10.3847/1538-4357/ab6f64](https://doi.org/10.3847/1538-4357/ab6f64)

Turner, B. E. 2001, *ApJS*, 136, 579, doi: [10.1086/322536](https://doi.org/10.1086/322536)

van der Tak, F. F. S., Black, J. H., Schöier, F. L., Jansen, D. J., & van Dishoeck, E. F. 2007, *A&A*, 468, 627, doi: [10.1051/0004-6361:20066820](https://doi.org/10.1051/0004-6361:20066820)

Yamamoto, S. 2017, *Introduction to Astrochemistry: Chemical Evolution from Interstellar Clouds to Star and Planet Formation*, doi: [10.1007/978-4-431-54171-4](https://doi.org/10.1007/978-4-431-54171-4)